Sensible heat fluxes control cloud trail strength

Received: 17 February 2022 | Revised: 4 February 2023 | Accepted: 10 February 2023 | Published on: 24 April 2023

DOI: 10.1002/qj.4438

Quarterly Journal of the Royal Meteorological Society RMetS

RESEARCH ARTICLE

Sensible heat fluxes control cloud trail strength

Michael C. Johnston[1] | **Christopher E. Holloway**[2] | **Robert S. Plant**[2]

[1]Guy Carpenter, Tower Place West, London, UK

[2]Department of Meteorology, University of Reading, Reading, Berkshire, UK

Correspondence
Michael C. Johnston, International Catastrophe Advisory, Guy Carpenter, Tower Place West, London, EC3R 5BU, United Kingdom.
Email: michael.johnston@guycarp.com

Funding information
NERC/Met Office (RevCon), Grant/Award Number: Grant/Award Number: NE/N013743/1

Abstract

Convective cloud bands known as "cloud trails" (CTs) are commonly found downwind of small islands (<O(100) km^2) throughout the world. They occur primarily in the afternoon, and are known to form in response to land–sea contrasts under the presence of background flow. A set of idealized numerical experiments with 100-m horizontal grid spacing is performed to quantify the relationship between the surface forcing produced by an island and the strength of the resulting CT circulation. These experiments are based on observed environmental conditions for which a CT occurred off Bermuda, a small subtropical island. For these simulations, the CT circulation is found to be controlled by the strength of the integrated excess heating of the flow as it passes over the island. This excess heating is in turn controlled by the strength of the island heat fluxes when the wind speed and the island geometry are kept constant. Our experiments show, all else equal, a linear relationship between CT circulation strength and the island surface heat flux.

KEYWORDS

convection-resolving models, idealized simulations, island convection, mesoscale circulations, surface heat fluxes

1 | INTRODUCTION

Bands of organized convective cloud, or "cloud trails" (CTs), can be found downwind of small islands around the world (e.g., Nordeen *et al.* (2001); Kirshbaum and Fairman, 2015; Johnston *et al.*, 2018). The daytime heating of small islands leads to a land–sea contrast in surface fluxes as the sea has a higher specific heat capacity than land. This horizontal variation in fluxes acts as a source for circulation generation, and the resulting circulations help organize cloud into the characteristic CT cloud bands (e.g., Matthews *et al.*, 2007; Kirshbaum, 2013; Kirshbaum and Fairman, 2015).

Cloud bands are readily observable with modern satellite imagery (e.g., Johnston *et al.*, 2018). Furthermore, circulation anomalies can be measured over an island with a dense enough observation network (Bhumralkar, 1973). However, it is much more difficult to observe the region downwind of the island where the bulk of the CT system resides. Dedicated observations made with aircraft for case study events have helped fill in some of these gaps and build a conceptual model of the downwind portion of the CT system. Malkus (1963) showed that the cloud band can become precipitating; Garstang *et al.* (1975) demonstrated that the island-warmed air forms a "warm plume" within the boundary layer extending tens of kilometers downwind of the island and likened it to urban heat islands; and Matthews *et al.* (2007) provided detailed observations of the temperature, humidity, and vertical velocity along the CT at various heights.

Previous work on CTs has revealed an island size and geometry dependence, and hints at the role of elevated heating and mechanical effects of mountains (Savijarvi and Matthews, 2004). When there is weak or no background flow, large heated islands (with diameter greater than 40 km) generate a traditional "sea-breeze" circulation while smaller heated islands generate a distinct but related "heat island" circulation (Savijarvi and Matthews, 2004). The resulting circulation regime can be predicted using a parameter that combines details of island size, background flow, and island heating — and the role of heating can be enhanced by mountains (Kirshbaum, 2013). However, all of these studies employ a relatively simplistic representation of turbulent processes and neglect moist physics in order to expand the conceptual model and understanding of island-driven circulations.

More complex models including moist physics have also been used to look specifically at CTs more recently. However, they often consider fairly mountainous real-world islands in experiments at resolutions considered fairly coarse for representing boundary layer processes. For example, CTs in the wake of the Hawaiian Islands were found to be formed by a combination of strong elevated heating modulated by flow splitting and re-forming in the wake of Hawaiian Islands in 1-km resolution simulations (Yang *et al.*, 2008). CTs past fairly mountainous islands in the Lesser Antilles were considered in 250-m and 500-m resolution experiments compared to satellite observations and found a strong relationship between island heating (focusing on elevated heating in particular) and updraught strength (Kirshbaum and Fairman, 2015). However, these are fairly large islands and the focus of these studies was primarily on impact of the mountains or elevated heating.

Furthermore, higher simulation resolution is required to adequately quantify the boundary layer and shallow convection circulation strength. To faithfully represent the shallow convection that characterizes CTs and indeed resolve the small island responsible for the convection, grid spacing of O(100) m is desirable (e.g., Stevens *et al.*, 2002; Cheng *et al.*, 2010; Honnert *et al.*, 2020; Johnston, 2020).

In the present study, we aim to quantify the relationship between a small, flat, heated island and the resulting CT circulation in a 100-m resolution numerical model. This is the highest resolution employed to consider CTs, and is intended to allow a more refined representation of boundary layer turbulence, shallow convection, and their relationship to the heated island in the absence of significant terrain. A case day with a persistent CT at Bermuda (a small, relatively flat island) is chosen as the subject of the experiments presented; this day is selected using an automated CT classification algorithm applied to visible satellite imagery following Johnston *et al.* (2018).

The current article is organized as follows: Section 2 describes the model, idealizations used, and the experimental design; Section 3 presents the results from those experiments; and finally conclusions are presented and discussed in Section 4.

2 | NUMERICAL SIMULATIONS

The main aim of this work is to expand on the established relationship between CTs and their island forcing. In order to do that, we use high-resolution numerical experiments within an idealized framework. These experiments are performed using the Met Office Unified Model, version 10.9 (the UM; Davies *et al.*, 2005) with a Cartesian coordinate system. This model solves non-hydrostatic dynamics for a deep atmosphere with semi-implicit, semi-Lagrangian advection. Sub-grid turbulence is treated with the blending approach of Boutle *et al.* (2014), which combines the 3D Smagorinsky–-Lilly scheme (Smagorinsky, 1963; Lilly, 1967) with the one-dimensional boundary layer scheme of Lock *et al.* (2000), using a transition function of the ratio between model grid spacing and boundary layer depth (including the cloud layer). Cloud formation assumes instantaneous condensation and the clouds simulated are non-precipitating.

2.1 | Model setup

The domain is chosen to be a channel-oriented east–west with $L_x = 118.4$ km by $L_y = 32.0$ km by $L_z = 40.0$ km in the Cartesian coordinates x, y, and z respectively. One hundred and forty vertical levels are used with vertical spacing of a few meters near the surface, and a mean spacing of about 40 m in the lowest 3 km where the majority of resolved convective and turbulent motions are expected to be contained. The lowest model level is 2 m. This high vertical resolution is intended to be adopted into operations for convection permitting local numerical weather prediction purposes (Bush *et al.*, in review). Damping is applied to the vertical velocity below the rigid upper boundary to absorb vertically propagating wave energy. Horizontal grid spacing of 100 m is used with biperiodic lateral boundary conditions.

Idealized prescribed forcing tendencies are also imposed, specifically a geostrophic forcing and a subsidence forcing. Without these idealized tendencies to the momentum, thermodynamic, and moisture budgets the effects of large-scale horizontal gradients could not be supported with biperiodic lateral boundary

conditions. Furthermore, a prescribed radiative cooling tendency is introduced in the thermodynamic budget. The geostrophic, subsidence, and radiative idealizations are applied as horizontally homogeneous vertical profiles. The full formulation of the imposed tendencies is given in Appendix A.

The role of the surface forcing in the CT system is being tested in this study and so we choose to prescribe sea surface and island surface fluxes. The sea surface fluxes are held constant in time and space (the values of these are given in Section 2.2), while the land surface fluxes are chosen to follow the diurnal cycle of Grabowski *et al.* (2006):

$$H(t) = \max\left[0, H_0 \cos\left(\pi \frac{(t_0 - t)}{T}\right)^{1.3}\right], \quad (1a)$$

$$E(t) = \max\left[0, E_0 \cos\left(\pi \frac{(t_0 - t)}{T}\right)^{1.5}\right], \quad (1b)$$

where $H(t)$ and $E(t)$ are the prescribed sensible and latent heat fluxes in $\mathrm{W{\cdot}m^{-2}}$ respectively, varying with time, t, in hours. H_0 and E_0 are the maximum values of the sensible and latent heat fluxes respectively, both in $\mathrm{W{\cdot}m^{-2}}$, and are reached at "midday", t_0, in hours. The length of the day in hours is given by T. In all experiments, we choose $t_0 = 12\,hr$ and $T = 12\,hr$. The surface is no-slip with roughness lengths $z_{0,\mathrm{sea}} = 10^{-4}$ m and $z_{0,\mathrm{land}} = 0.5$ m, the latter being representative of Bermuda.

2.2 | Initial conditions

The initial conditions used are based on wind and thermodynamic profiles from a selected CT day at Bermuda. We are not attempting to reproduce the observed CT, but the fact that these conditions are known to result in the formation of a persistent CT makes them suitable for the purposes of these experiments.

Initial conditions used in each experiment are found using a "spin-up" simulation performed on a smaller 3.2 km × 3.2 km domain for 10 simulated days without an island. This is intended to be long enough for the initial thermodynamic and wind profiles (introduced below) to come into balance with idealized forcing tendencies and a constant sea surface temperature. The horizontal-mean, time-mean profiles over the spin-up domain and the last four days of the spin-up simulation are taken as the initial conditions for the experiments. In addition, the same horizontal mean and time mean are applied to the sea surface sensible and latent heat fluxes which are prescribed as constant in all experiments.

Given there could be meaningful changes to the environment due to the CT itself, achieving a quasi-balanced state between initial conditions and idealized forcing tendencies is desirable for separating the effects of the CT from the chosen idealizations. Furthermore, this allows us to assume negligible evolution of the large-scale state and isolate the role of the heated island on CT formation and evolution.

The radiosonde observations from Bermuda (ICAO: TXKF) on the morning of July 16, 2015 are chosen to form the basis for our experiments as this is a day in which a persistent CT was identified in visible-channel satellite imagery using the automated procedure outlined in Johnston *et al.* (2018).

The observed thermodynamic profiles in the 09:00 local time (1200 UTC) radiosonde ascent on this day are simplified by splitting the temperature and relative humidity profiles into the following meteorologically relevant layers: a "well-mixed layer" from the surface to about 600 m; a "cloud layer" from about 600 m to about

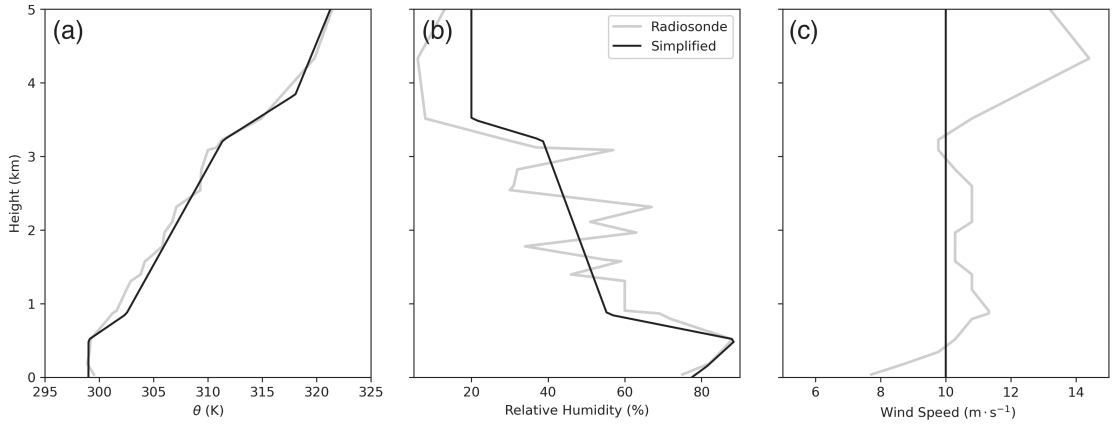

FIGURE 1 The observed radiosonde profiles in gray and simplified profiles in black of potential temperature in (a); relative humidity in (b); and wind speed in (c)

3.2 km; and the "free troposphere" from 3.2 to about 15 km (see Figure 1a,b). Transitions are retained between the well-mixed layer and the cloud layer, and between the cloud layer and the free troposphere. The observed wind profile is simplified to be unidirectional with height, easterly, and 10 $m \cdot s^{-1}$ (Figure 1c).

On this day, the Bermuda Weather Service reported a near-shore sea surface temperature of 29.3°C, and this is taken as the sea surface temperature for the spin-up simulation. From the spin-up simulation, we find that the balanced sea surface sensible heat flux is 1.5 $W \cdot m^{-2}$ and latent heat flux is 167.2 $W \cdot m^{-2}$. These sea surface flux values are prescribed as constant in time in our experiments described in the next section (Section 2.3).

Since easterly flow is prescribed, it is convenient to place the island towards the eastern boundary of the domain. The island is circular and centered at $x = 108$ km, $y = 16$ km with an area of 50 km^2 (diameter of about 8 km). For islands of this size, CTs have been observed to be around 100 km long (e.g., Nordeen *et al.*, 2001; Johnston *et al.*, 2018). Thus, the simulated CT is expected to extend from near the island across the remaining length of the domain.

2.3 | Experiments

A suite of experiments is presented in which the island surface fluxes are controlled and varied, keeping all else equal. Surface sensible heat fluxes are expected to be the dominant driver of the CT system based on previous work and observations. The role of sensible heat flux is explored by varying the values at time of peak heating, H_0, from 50 to 400 $W \cdot m^{-2}$ in 50 $W \cdot m^{-2}$ increments while the latent heat flux at the time of peak heating, E_0, is kept constant at 250 $W \cdot m^{-2}$. A mid-range experiment is chosen as a "control" with $H_0 = 250\ W \cdot m^{-2}$. Previous studies have used 150 $W \cdot m^{-2}$ (Kirshbaum and Fairman, 2015), and 250 $W \cdot m^{-2}$ (Jahn *et al.*, 2016) for larger islands.

In varying H_0 but keeping E_0 the same, the total turbulent energy flux ($Q = H + E$) is not kept constant between experiments. Additional experiments (H125E375 and H375E125) are considered where Q at the time of peak heating is kept constant, but H_0 and E_0 are repartitioned. This changes the Bowen ratio, $\beta = H/E$, and is intended to assess the sensitivity of the CT system to surface latent heat fluxes and to the change in total energy flux. All of the experiments are summarized in Table 1.

Each experiment has the same initial conditions and forcing tendencies and is run for 24 hr. The diurnal cycle of surface heating over the island starts at hour 6, peaks at hour 12, and ends at hour 18. This experiment construction captures the pre-heating state, the daytime heating cycle, and several hours after sunset. The island is not heated (i.e., $H = E = 0\ W \cdot m^{-2}$) from 0000 to 0600 hr, and from 1800 to 2400 hr.

TABLE 1 An index of the experiments performed, listing the peak sensible and latent heat fluxes over the island. Experiments marked with an asterisk (*) test differences in Bowen ratio by keeping the same total turbulent energy flux (sensible plus latent) as the control, and varying the partitioning between the two

Experiment ID	Sensible heat flux, H_0 ($W \cdot m^{-2}$)	Latent heat flux, E_0 ($W \cdot m^{-2}$)
H050E250	50	250
H100E250	100	250
H125E375*	125	375
H150E250	150	250
H200E250	200	250
H250E250 (control)	250	250
H300E250	300	250
H350E250	350	250
H375E125*	375	125
H400E250	400	250

3 | RESULTS

In this section, the results of the suite of experiments will be presented and discussed. Section 3.1 discusses the "control" experiment (labeled as H250E250 in Table 1) and introduces the behavior and structure of the idealized CT system. Section 3.2 analyses some key elements of the CTs in the context of the full suite of experiments. One focus is the relationship between the chosen peak island sensible heat flux, H_0, and the strength of the induced circulation, but additional experiments are also discussed, including experiments which varied the latent heating, to facilitate a more complete understanding of the CT system.

3.1 | Control experiment

For an overview of the CT evolution in the control experiment, we consider the cloud field derived from the liquid water path (LWP, the vertical integral of simulated cloud liquid water, q_c) and the 10-m wind field decomposed into components, s, along the flow (i.e., parallel to the initial horizontal mean wind vector at 10 m), and n, across the flow (i.e., orthogonal to s). Snapshots of these wind components during the first few hours of island heating are

used in Figure 2 help to visualize the low-level circulation during the initial CT formation.

Prior to hour 6, a field of ambient scattered shallow cumulus cloud forms over the sea which is heated at a constant rate. The island has surface energy fluxes set to zero, lower than the surrounding sea, and a higher surface roughness. As a result, a wake of decelerated, more stable air forms and extends roughly 20 km downwind. This wake manifests as an area of suppressed cloud formation (not shown). At hour 6, the island is heated and the stability anomaly in the wake of the island rapidly reverses allowing cloud cover similar to the background cloud field to fill in (Figure 2a). By hour 9, the first signs of the CT begin to emerge in the form of a somewhat disorganized plume of enhanced cloud formation with higher LWP and higher cloud top heights (darker shading indicating higher LWP to the left of the island in Figure 2b). A characteristic cloud band consolidates by hour 11 and persists until hour 18, the remainder of the time that the island is heated (e.g., cloud band between $x = 20$ and 70 km at hour 12 in Figure 2c). This simulated CT is visually comparable to satellite images of CTs identified on real-world islands (e.g., as reported by Nordeen *et al.*, 2001 and Johnston *et al.*, 2018).

Since individual clouds within the cloud band are intermittent, we also consider a time-averaged view of the cloud field. First, the LWP is converted to a cloud mask with model output every minute by taking any LWP value greater than 0 $g \cdot m^{-2}$ to indicate the presence of cloud. The cloud masks are then averaged in time from hour 6 to hour 18 covering the period in which the island is heated. This process results in a two-dimensional field of the cloud frequency as a fraction of 1-min frames for which there is cloud.

A rectangle oriented into the boundary layer mean wind direction is then defined. The mean boundary layer wind is from the eastnortheast as it is backed from the prescribed easterly geostrophic wind due to surface drag. The cloud frequency is averaged in the n direction (across the short axis of the rectangle), and plotted in the s direction (along the long axis of the rectangle, in distance downwind) in Figure 3a. The length of the short side of the rectangle matches the island diameter (8 km). The long side extends from one island diameter upwind of the windward edge of the island to 100 km downwind of the island.

Several structural features become clearer from this time-averaged perspective, a map of which is also shown in Figure 3b. Key features are annotated (in order from near the island with increasing distance downwind): a "turbulent cloud patch" in the immediate wake of the island and extending up to 20 km downwind; a cloud "void" between 20 and 40 km downwind of the island; and the "main cloud band" starting roughly 40 km downwind of the island and extending tens of kilometers farther downwind.

These three regions correspond respectively to the broad cloud patch which forms around hour 9 in the simulation (Figure 2b), a transition region with a "void" or break in the cloud signature, and a more organized band of cloud (Figure 2c).

To explain this structure, we consider a snapshot of the across-flow component of the 10 m wind, n', at hour 12 in the simulation (where positive n' points northnorthwestward) in Figure 4a. This highlights a long trail of low-level across-flow convergence extending from the leeward side of the island along the length of the CT region. The inflowing branches have n' typically of 1 to 2 $m \cdot s^{-1}$.

Furthermore, we reveal the near-surface warm plume with the 2-m potential temperature anomaly with respect to the horizontal mean potential temperature, $\theta' = \overline{\theta} - \theta$, in Figure 4b. The warm plume takes the form of a triangular-shaped region of higher θ' in the immediate wake of the island, with θ' up to 1°C and narrowing with distance from the island. The warm plume narrows from a width of roughly one island diameter near the leeward side of the island, forming the point of the triangle and disappearing roughly 40 km downwind of the island.

While the across-flow component of the wind is generated at or near the island, the background flow in our experiments advects the air downwind of the island before the low-level inflowing air from the flanks of the island meets. Inflowing air on either side would need to travel approximately an island radius to meet the opposing branch. In our experiments, the island radius is about 4 km and typical inflow, n', is of order 1 $m \cdot s^{-1}$. It would therefore take roughly 4,000 s for the inflow from either side to meet in the middle. During that time, the background flow (approximately 10 $m \cdot s^{-1}$) would carry these anomalies 40 km downwind before they meet, leading to the triangular surface warm plume seen in Figure 4b.

Near-surface-based parcels originating over the island and in the first few kilometers of the warm plume are positively buoyant well into the cloud layer. In order to visualize areas along the CT where surface-based parcels are positively or negatively buoyant as they rise, the difference between the surface potential temperature and the local environmental potential temperature ($\theta - \theta_{sfc}$) is shown as a snapshot in time in Figure 5a. Here, regions of the boundary layer and overlying cloud layer in which a surface-based parcel is positively buoyant appear blue, and a blue region over the island is revealed in Figure 5a. This suggests that clouds are being initiated due to disorganized buoyant motions over the island. Given the typical life-time of shallow convective cloud of around half an hour (10 to 45 min, sections 1.3.3 and 1.3.4 of Cotton

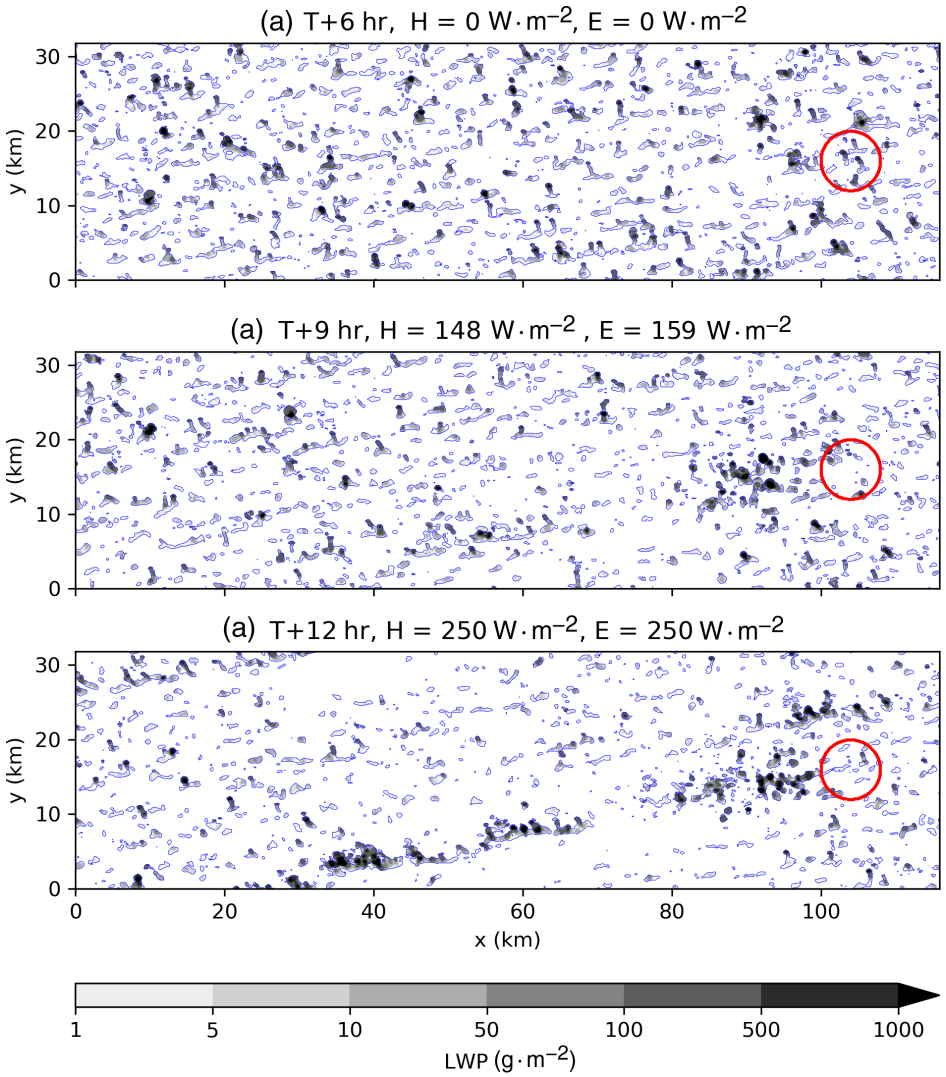

FIGURE 2 Snapshots of the liquid water path (LWP) in g·m^{-2} in grayscale shading. A contour of LWP = 0 g·m^{-2} is outlined, and the island coastline is outlined as a circle to the right hand side of each panel. Snapshots are shown after (a) hour 6, (b) hour 9, and (c) hour 12, with the corresponding values of surface fluxes over the island noted in each panel's title [Colour figure can be viewed at wileyonlinelibrary.com]

and Anthes, 1989) and background flow at 10 m·s^{-1}, clouds formed over the island would travel roughly 18 km downwind of the island. This mechanism fully explains the turbulent cloud patch we see presented in Figures 2 and 3.

The inflowing components also advect in air from either side near the surface and undercut the warm plume. This leads to a more stably stratified boundary layer structure with cooler ambient air near the surface and island-warmed air near the top of the boundary layer. Near-surface air parcels lifted by the CT circulation in this region encounter more resistance as they become negatively buoyant before reaching their lifting condensation level (LCL) and therefore fewer clouds form here. This is illustrated in Figure 5a where the thin black line representing the boundary layer height is lower than the heavy black line representing the height of the LCL. This configuration extends approximately 30 to 40 km downwind of the island.

The LCL is given as the heavy line, and the mixed layer depth is given as the thin line in Figure 5. The height of the LCL is found following Bolton (1980):

$$P_{\mathrm{LCL}} = P_{\mathrm{sfc}}\left(\frac{T_{\mathrm{LCL}}}{T_{\mathrm{sfc}}}\right)^{\frac{c_{\mathrm{pd}}}{R_{\mathrm{d}}}}, \tag{2a}$$

$$T_{\mathrm{LCL}} = \frac{1}{\frac{1}{T_d - 56} + \frac{\ln\left(\frac{T_{\mathrm{sfc}}}{T_{\mathrm{d}}}\right)}{800}} + 56, \tag{2b}$$

where P_{LCL} is the pressure at the height of the LCL in hPa, P_{sfc} is the surface pressure in hPa, T_{LCL} is the temperature at the height of the LCL in Kelvin, T_{sfc} is the surface air temperature in Kelvin, c_{pd} is the specific heat capacity of dry air at constant pressure taken as 1,005 J·kg^{-1}·K^{-1}, R_{d} is the gas constant for dry air taken as 287.05 J·kg^{-1}·K^{-1}, and T_{d} is the surface air dewpoint temperature in Kelvin. Surface air temperature and

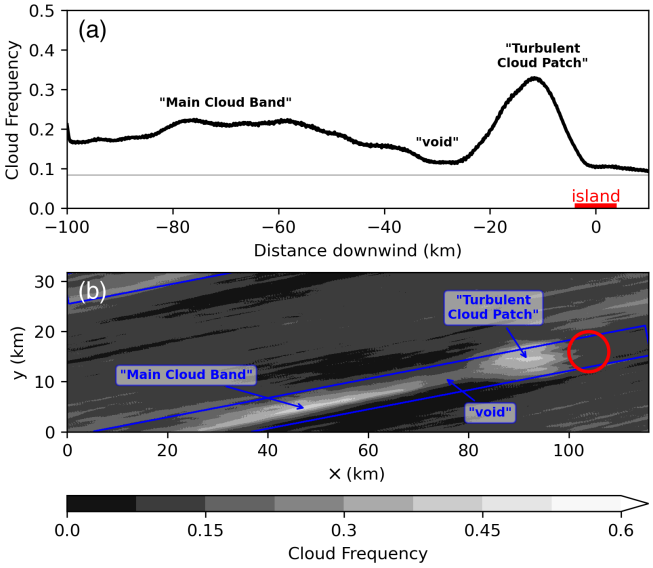

FIGURE 3 The daytime (hours 6 to 18 model time) cloud frequency in the control simulation. (a) As a function of distance away from the leeward edge of the island; and (b) the spatial distribution of cloud frequency. The cloud frequency in (a) is found by averaging in the direction of the short axis of the rectangle in (b), that is, in the direction normal to the domain mean boundary layer flow. A gray horizontal line in (a) denotes the spatial mean daytime cloud frequency outside of the cloud trail (CT) region and represents the background cloud frequency. The location of the island is highlighted as a line labeled "island" in a) and as a circle in panel b). [Colour figure can be viewed at wileyonlinelibrary.com]

dewpoint temperature are both taken at the lowest model level (2 m).

To further highlight the warm plume being undercut, and shoaling/thinning with distance downwind of the island, we consider anomalies of the quantity displayed in Figure 5a from its horizontal mean. A snapshot of this field is presented in Figure 5b where blues indicate that a surface-based parcel is more positively buoyant at that location than the horizontal mean at that height, and reds indicate a surface-based parcel is more negatively buoyant. As expected, surface-based parcels originating over the island are much more negatively buoyant than average. However, a more nuanced result is that surface-based parcels downwind of the island are anomalously more negatively buoyant as they rise through the boundary layer. This region of anomalous negative buoyancy to surface-based parcels coincides with the region identified as having a cloud void in Figure 3.

The cloud band emerges more than 40 km downwind of the island. Here, convective cloud originating over the island (associated with the turbulent cloud patch) has dissipated, and the CT circulation has eroded the warm plume enough to overcome the negative buoyancy it imposes on surface-based parcels so that the ascending branch of the CT circulation can trigger cloud formation along a concentrated region of convergence.

We present these three components of the CT system in a schematic (Figure 6). The across-flow components of the system are shown in Figure 6a, while the along-flow components of the system are shown in Figure 6b. This schematic synthesizes analyses of numerical simulations of small heated islands and heated isolated hills presented by Savijarvi and Matthews (2004) and Kirshbaum (2013) with surface and aircraft observations by Malkus (1963), Bhumralkar (1973), Garstang *et al.* (1975), and Matthews *et al.* (2007). A schematic showing the downwind circulation and cloud structure for CTs on Nauru was produced for the COMET website (accessed 2017) based on aircraft observations from Matthews *et al.* (2007). The present work expands upon this body of previous work by including new details of the warm plume and its relationship to a cloud void.

We find it helpful to discuss the CT system in terms of the baroclinically generated horizontal vorticity components (i.e., the vorticity vectors which point parallel to the ground). Here, the land–sea contrast in heating induces a horizontal buoyancy gradient which can be shown to be proportional to the baroclinic or "solenoidal" generation term of the vorticity equation in the orthogonal direction, that is:

$$\frac{\partial \omega_x}{\partial t} \propto \frac{\partial b}{\partial y}, \tag{3}$$

where $\partial\omega_x/\partial t$ is the horizontal vorticity tendency in the x-direction, and $\partial b/\partial y$ is the horizontal buoyancy gradient in the y-direction. In the absence of background flow, the resulting circulation in Equation (3) has flow components pointing toward the island near the surface, ascending, then pointing away from the island at some height and descending, forming a traditional sea-breeze circulation. However, the sea-breeze circulation is transformed into what Savijarvi and Matthews (2004) described as a "heat island circulation" given sufficiently strong background flow, where island size matters for what is considered "sufficiently strong". The schematic in Figure 6 is constructed following the control (H250E250) experiment in the present work.

Figure 6a considers the heat island circulation from the perspective of an observer looking downwind at a heated island (i.e., with the background flow into the page). In this view, the expected traditional sea-breeze circulation couplet forms either side of the island. This is associated with low-level convergent inflow, ascent over the island, and divergent outflow at a higher altitude. In our experiments, the outflow is found near and above the top of the boundary layer. Circular arrows left and right of the

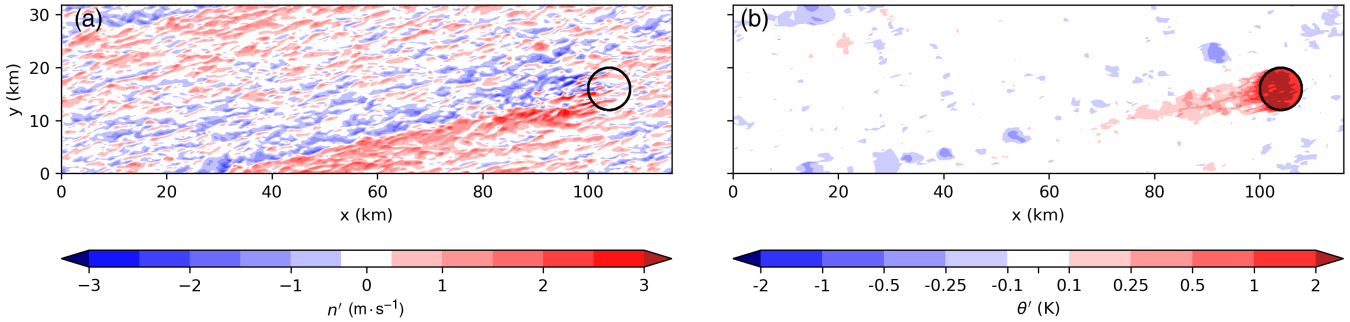

FIGURE 4 Snapshots after 12 simulated hours of the 10-m wind component across the flow (n', orthogonal to the horizontal mean wind vector at this height) in (a), and the 2 m potential temperature anomaly with respect to the horizontal mean potential temperature at this height (θ') in (b) [Colour figure can be viewed at wileyonlinelibrary.com]

island in Figure 6a indicate the sense of vorticity associated with the in–up–out circulation. Here, '–' indicates a horizontal vorticity vector pointing out of the page with a counter-clockwise sense of circulation around it, and a "+" denotes horizontal vorticity vector pointing into the page with a clockwise sense of circulation around it. In contrast with the sea-breeze system where the circulation remains near the coastline, the circulation generated at the coastline is advected downwind supporting a band of low-level convergence. Finally, the relatively higher sensible heat flux associated with the island leads to the formation of a "warm plume" as described by Garstang *et al.* (1975) which is aligned with the island in this perspective.

In Figure 6b, we consider the heat island circulation from the perspective of an observer looking at the island across the flow, that is, with the background flow from right to left. In this perspective, the traditional sea-breeze circulation is completely transformed: the horizontal vorticity couplet is advected downwind such that the negative pole continues downwind to the left where it is cut off from the buoyancy gradient and dissipates as indicated by the faded circular counter-clockwise arrow on the far left of Figure 6b. The positive pole progresses across the island where it becomes phase-locked to the leeward side of the island as indicated by the circular clockwise arrow to the left of the island and within the orange-shaded warm plume in Figure 6b. This process is also described in more detail in section 4a of Savijarvi and Matthews (2004). Downwind of the island, the region of clockwise vorticity is "tilted" or misshapen such that the outflow near the top of the boundary layer is farther downwind than the inflow near the surface because of vertical wind shear within the boundary layer due to surface drag (note that this is not referring to tilting a horizontal vorticity vector such that it has a component pointing in the vertical). While not necessarily relevant to the individual components of the CT system, this portion of the vorticity and associated wind perturbation vectors are retained to help understand how the sea-breeze circulations are transformed into the heat island circulations.

The narrowing of the warm plume with distance downwind from the island (as demonstrated experimentally in Figure 4) is illustrated in Figure 6b with the "triangular surface warm plume". Furthermore, the stabilization of the boundary layer downwind of the island with respect to ascending surface-based parcels due to the warm plume being undercut by inflowing air (as demonstrated experimentally in Figure 5) is illustrated in Figure 6b with the warm plume being farther downwind at heights near the top of the boundary layer than near the surface with the resulting cloud "void" above.

For the remainder of the presented experiments, the majority of analysis is designed to focus on the cloud band portion of the downwind CT system. This low-level feature is a dynamical response to the island heating and extends tens of kilometers downwind of small islands where it can organize and trigger new convection. With an extent of around 100 km downwind, the CT circulation demonstrates non-local convective behavior where convection is triggered far from the source of triggering. This mechanism could be of particular interest for the development of convection parameterizations in models with horizontal grid spacing of order 10 km and for situations involving heterogeneous surface heating (e.g., islands, lakes, and cities).

3.2 | Circulation strength

The CT circulation which forms in the wake of a heated island has been shown above and in previously cited work to be a direct dynamical response to the land–sea contrast which arises from the more pronounced diurnal cycle over the island. Here, we seek to present changes to the resulting cloud field and quantify the relationship between peak

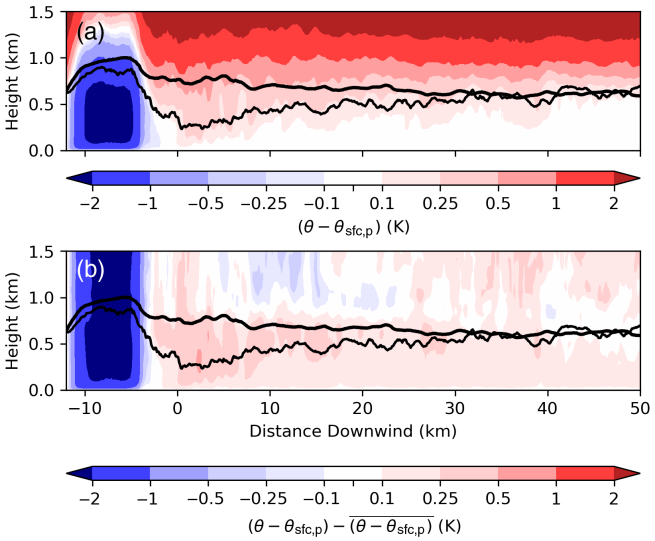

FIGURE 5 Instantaneous snapshot at hour 12 ("midday") of the height–distance downwind cross-sections of the potential temperature difference between a surface-based parcel ascent and the environment in (a), and anomalies of that quantity from its horizontal mean in (b). The surface-based parcel ascent is denoted by the subscript "sfc, p". Negative values in (a) indicate a surface-based parcel is positively buoyant with respect to the environment at that height and location, while positive values indicate the parcel is negatively buoyant. Negative values in (b) indicate a parcel is more positively buoyant at that height and location than average at that height, while positive values indicate the parcel is less buoyant than average. Positive distance downwind indicates locations to the westsouthwest of the island. The height of the lifting condensation level (LCL) is marked with a heavy black line, and the height of the mixed layer is marked with a thin black line. Both LCL and mixed layer heights are instantaneous, without spatial averaging. All diagnostics are with respect to an air parcel taken at the lowest modeled level: 2 m height [Colour figure can be viewed at wileyonlinelibrary.com]

island surface heat flux and the mass flux near cloud base within the resulting CT's cloud band.

Figure 7 presents the time-mean cloud field diagnostics for each of the $E_0 = 250\ \mathrm{W \cdot m^{-2}}$ experiments outlined in Table 1. Individual line plots in Figure 7 are constructed following the method introduced for Figure 3a. As the island sensible heat flux increases, so does the cloud frequency in the turbulent cloud patch region (between −20 and 0 km in Figure 7). Moreover, the cloud "void" narrows slightly and becomes less distinguishable from the main cloud band as peak island heat flux increases. For the lowest heat flux experiment, H050E250 with $50\ \mathrm{W \cdot m^{-2}}$, the cloud band cloud frequency is only slightly higher than the cloud frequency upwind of the island. Furthermore, the peak cloud frequency in the cloud band migrates closer to the island for higher peak island heat flux (from −80 km in H050, to −60 km km in H400). These results match the expected direction of the relationship between island heat flux and the visible behavior of the CT system as discussed in the previous section and from previous work on idealized dry heated islands in Kirshbaum (2013).

Using scaling arguments, we can determine the expected relationship between surface heat fluxes and CT circulation strength. In the previous section's description of the CT system, we use horizontal vorticity and advection arguments in an across wind-vertical plane (e.g., Figure 6a) to conceptualize the formation of the cloud band. From this viewpoint the horizontal vorticity, ω_x, is assumed to be primarily generated by the horizontal buoyancy gradient across the flow as in Equation (3). We can approximate the strength of the buoyancy perturbation caused by the island as:

$$b' = g\frac{T'}{T_0}, \tag{4}$$

where b' is the buoyancy perturbation, g is the acceleration due to gravity, T' is the temperature perturbation, and T_0 is the ambient temperature. The temperature perturbation is produced by heating the air as it passes over the heated island. Assuming that the island heating is distributed evenly through the depth of the boundary layer and that the boundary layer depth does not materially change, the temperature perturbation of the air after passing over the island can be given as:

$$T' = \frac{Hl_x}{\rho c_{pd} z_h U}, \tag{5}$$

where H is the sensible heat flux, l_x is the island width in the along-wind direction, z_h is the boundary layer depth, ρ is the air density, c_{pd} is the specific heat capacity of dry air at constant pressure, and U is the ambient wind speed. This reflects the heating input at the surface ($H/\rho c_{pd}$) being distributed through the depth of the boundary layer (z_h) over the residence time of air over the island ($\Delta t = l_x/U$).

Substituting Equations (4) and (5) into Equation (3), and using $\partial y \sim \Delta y = l_y/2$ (where l_y is the width of the island in the across-flow direction) we get the following:

$$\frac{\partial \omega_x}{\partial t} \propto \frac{2gHl_x}{\rho c_{pd} z_h U T_0 l_y}, \tag{6}$$

Integrating the relationship given by Equation (6) with respect to the residence time, one would expect the strength of the horizontal vorticity generated to be directly proportional to the heat flux: $\omega_x \propto H$.

Applying similar reasoning to the vertical momentum equation and integrating in time, it can also be shown that

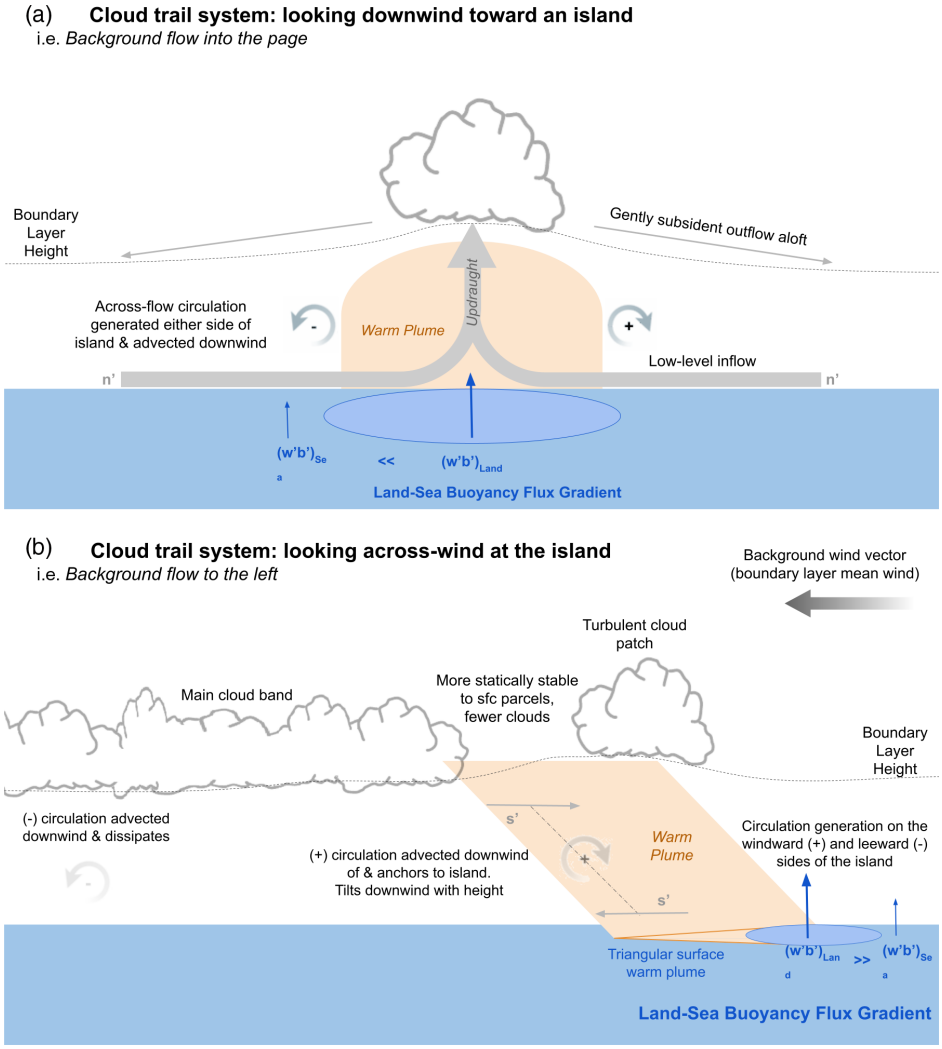

FIGURE 6 A schematic diagram of the main features of the Cloud Trail System as identified in this section. (a) The across-flow system where the land–sea contrast in surface buoyancy fluxes generates a convergent low-level circulation at and downwind of the island similar to the traditional sea-breeze. Cloud forms over and downwind of the island, particularly atop the ascending branch of the across-flow circulation. (b) The along-flow system where the traditional sea-breeze circulation is advected downwind and transformed into the "heat island circulation" (Savijarvi and Matthews, 2004). The main cloud band is supported by the across-flow circulation from (a) which is also advected downwind from the island, while, at least in the Control simulation, the cloud band and turbulent cloud feature are separated due to along-flow variations in stability and in the dominant mechanisms for ascent as described in more detail in the main text. [Colour figure can be viewed at wileyonlinelibrary.com]

the resulting updraught vertical velocity strength varies with H for example:

$$w \propto b'\Delta t = \frac{gHl_x^2}{\rho c_{pd} z_h T_0 U^2}, \tag{7}$$

In order to measure the strength of the CT, we introduce a diagnostic for the mean updraught mass flux at cloud base in the cloud band, or "CT updraught mass flux", M_c. This diagnostic integrates the updraught vertical velocity which we have related to heat flux in Equation 7 along the length of the CT and is defined as:

$$M_c = \frac{1}{S}\int_s\int_n < w\rho > ds\, dn\,, \tag{8}$$

where M_c has units of kg·m^{-1}·s^{-1}, S is the length of the rectangle over which the integration is performed in m, w is the upward vertical velocity at the height of the LCL in m·s^{-1}, ρ is the air density at the height of the LCL in kg·m^{-3}, $< w\rho >$ is the time-mean mass flux at the height of the LCL in kg·m^{-2}·s^{-1} and ds and dn are in the s and n directions of the rotated coordinate system such that s is parallel to the low-level flow and n perpendicular. The integral is evaluated at the domain mean height of the LCL which is taken as the approximate height of the cloud base.

M_c is averaged in time between hour 9 and hour 12. This timeframe captures the initial development and maturation of the CT's main cloud band and avoids potential recirculation of the CT system through the domain's periodic boundary conditions. The rectangle in which M_c is computed is 6 km wide which is wide enough to encompass the cloud band, and the rectangle extends approximately 95 km downwind of the island — this distance is determined by taking the mean boundary layer wind speed (8.8 m·s^{-1}) multiplied by the 3-hr averaging period. The turbulent cloud patch and cloud void areas in the immediate wake of the island are not included in the calculation by truncating the rectangle by an island diameter (8 km) downwind of the island. This area is not included as the turbulent cloud plume is formed through a separate

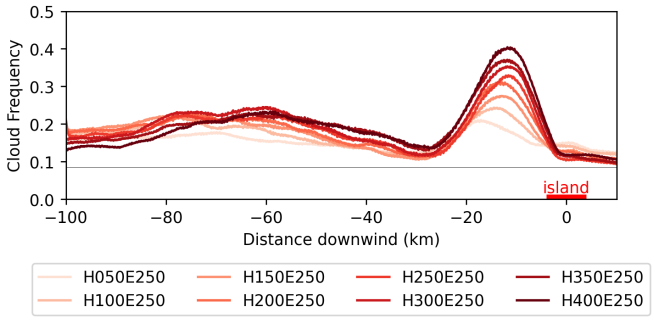

FIGURE 7 The daytime (0600–1800 hr model time) cloud frequency for the experiments in Table 1 with $E = 250\,\mathrm{W{\cdot}m^{-2}}$, computed as in Figure 3 as a function of distance away from the island midpoint. The gray horizontal line denotes the horizontal-mean, time-mean daytime cloud frequency outside the cloud trail (CT) region for the control experiment (H250E250), and represents the ambient cloud frequency. The island location relative to each curve is annotated. [Colour figure can be viewed at wileyonlinelibrary.com]

mechanism to the cloud band and is not the subject of the current investigation.

In Figure 8, M_c for each experiment is compared against the maximum total net surface energy flux, $Q_{net} = H_0 + E_0$ in Figure 8a, against H_0 in Figure 8b, and against the surface buoyancy flux, $\frac{g}{\theta_{v,0}}\left(\overline{w'\theta'_v}\right)_0$, in Figure 8c. The strength of the CT circulation is shown to increase linearly with surface heating over the range of experiments. In Figure 8a, we see that the two experiments varying the Bowen Ratio while keeping Q_{net} constant diverge from the line of best fit for M_c against Q_{net}, while they lie closely along the line of best fit for M_c against H_0 in Figure 8b. The quality of the fit is also very similar against the surface buoyancy flux in Figure 8c as buoyancy fluxes are more strongly driven by the sensible heating rather than latent heating. These results indicate that the cloud band circulation strength is predominately explained by H_0 alone, and the contribution of E_0 and moisture are negligible. Furthermore, these results support the assertion that M_c, and therefore w, vary linearly with H which matches our expectations from scale analysis presented above.

Our line of best fit does not pass through the origin when plotted against Q_{net} in Figure 8a, H_0 in Figure 8b, or the buoyancy flux in Figure 8c. We can demonstrate that the intercept at zero island surface flux represents the updraught mass flux related to the ambient cloud field (not shown). Over the 3-hr period from 0300 to 0600 hr, prior to island heating and CT formation, the mean updraught mass flux in the domain is $0.48\,\mathrm{kg{\cdot}m^{-2}{\cdot}s^{-1}}$. This corresponds to an M_c of $166\,\mathrm{kg{\cdot}m^{-1}{\cdot}s^{-1}}$ over the rectangle used to evaluate our experiments, which is of similar magnitude to the intercept of the best fit line at $H_0 = 0\,\mathrm{W \cdot m^{-2}}$. We therefore assert that the non-zero intercept represents the ambient updraught mass flux integrated within our rectangle of investigation following Equation (8). Note that if the updraught mass flux for the cloud band was isolated from other updraughts one would expect the intercept to be zero.

4 | DISCUSSION AND CONCLUSIONS

This article marks the first set of experiments using a high-resolution numerical model specifically to explore the CT system on small flat islands ($50\,\mathrm{km^2}$ in this case). We identify and fully describe a warm plume, turbulent cloud patch, a relative cloud void, and thermally driven circulation which organizes the characteristic CT cloud band. The turbulent cloud patch and the cloud band have been studied both observationally and with idealized numerical experimentation to construct conceptual models of the general circulation response. However, the warm plume has not been well addressed and the cloud void has not been studied in any detail prior to the present work.

We find that the turbulent cloud patch in the immediate wake of the island can be explained from buoyant cloud forming over the island and advecting downwind where it dissipates at the end of a typical cloud lifetime of about half an hour. A warm plume containing air heated over the island narrows and is eroded from underneath by low-level inflowing branches of the CT circulation. A cloud void then forms from a nuanced interplay between the role of the warm plume on the stability of surface-based air parcels and the ability of the CT circulation to lift low-level air to the LCL. The void ends and the cloud band begins where the CT circulation has eroded away the capping overrunning layer of the warm plume. The existence of the cloud void therefore depends on the strength of the island heating (which intensifies the CT circulation but also intensifies the warm plume), and the background wind speed (which determines how far downwind the warm plume gets before being undercut by the CT circulation). For larger, more mountainous islands, a similar cloud void could potentially arise from flow separation or mountain wave-breaking in the wake of a mountain in specific stability regimes, and a similar cloud band could form through baroclinic generation of horizontal vorticity that is tilted into the vertical as flow is deflected by the mountain (Lin, 2007).

The CT circulation is further considered through the lens of convection parameterization as we introduce the CT updraught mass flux diagnostic, M_c, as a measure of CT circulation strength. We show that

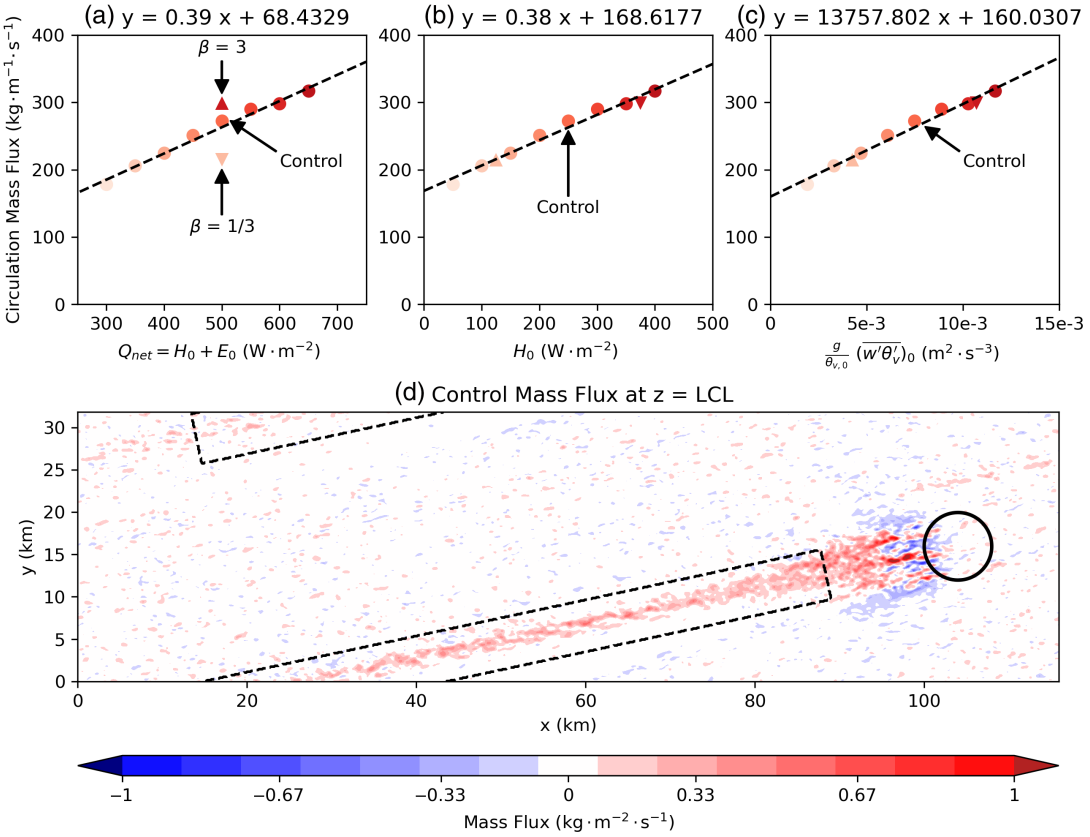

FIGURE 8 The circulation mass flux, M_c, is plotted against (a) peak island total turbulent surface energy flux, Q_{net}, (b) peak island surface sensible heat flux, H_0, and (c) peak island surface buoyancy flux. A line of best fit is drawn as a dashed black line and the equation for the line of best fit is reported in each panel's title. The symbols are shaded a darker for higher H_0 in each experiment, and are circular for experiments where only H_0 changes, and are triangular for experiments where the Bowen ratio, β, changes with Q_{net} kept constant. An example of the time-mean mass flux two-dimensional field, averaged between hours 9 and 12, at the height of the lifting condensation level (LCL) is shown for the control simulation in (d). Also in (d), a bold black circle represents the island coastline, and a dashed rectangle represents the area over which M_c is computed [Colour figure can be viewed at wileyonlinelibrary.com]

changes to the peak island daytime surface sensible heat flux, H_0, explain nearly all of the change in M_c for a given background wind speed and island geometry. For convection parameterization developers considering the effect of small islands on convection triggering and evolution at distances far downwind, this result implies that cloud base mass fluxes downwind depend only on the island geometry, the land–sea contrast in sensible heat flux, and the low-level wind speed. Given mechanistic similarities between CTs and other phenomena such as lake-effect snow (or any circulations arising from surface heterogeneities), there is reason to believe that this result is potentially extensible to plethora cases.

The relationships between the CT circulation strength and island heating reported in this paper also extends existing work. Compared to maximum updraughts at cloud base for Dominica in Kirshbaum and Fairman (2015), the updraughts associated with our idealized small island are much stronger and occur closer to the island. These differences are likely in part due to the higher model resolution employed in our experiments which allows better representation of narrow updraughts, and because the size of a heated island is inversely related to the resulting updraught strength (as shown by e.g., Savijarvi and Matthews, 2004 and Kirshbaum and Fairman, 2015). For decreasing island size, the net heating of a low-level parcel following the flow across the island decreases as there is less time spent over the island heat source. However, for decreasing boundary layer depth, - resulting in stronger thermal perturbation and therefore updraught strength. This implies an aspect ratio between the island size and the boundary layer depth the implied updraught strength increases as the vertical aspect ratio between the island size along the flow and the boundary layer depth increases because the layer over which the heating is distributed is shallower. This balance of factors suggests the existence of an optimized island-size wind speed combination that maximizes updraught strength.

Finally, the present work finds that $M_c \propto w_{CT} \propto H^1$. This result appears to be at odds with results previously reported in Kirshbaum and Fairman (2015) where $w_{CT} \propto H^{0.5}$. However, there are significant methodological differences between the present study and Kirshbaum and Fairman (2015). Kirshbaum and Fairman (2015) use Buckingham's Pi Theorem. This theorem allows one to arrive at an empirical scaling relationship by fitting experimental data to a power-law function of the form $w_{CT} = d_w \Pi_1^{a_w} \Pi_2^{b_w}$, where d_w, a_w, and b_w are coefficients to be fit. Kirshbaum and Fairman (2015) chose $\Pi_1 = z_h/l_y$ and $\Pi_2 = gHl_x^3/\rho c_{pd} T_0 U^3 l_y^2$ which are functions of physical variables determined using "dimensional analysis." It should be highlighted that $b_w = 0.5$ is applied to the whole function, Π_2 (including variables other than H), in Kirshbaum and Fairman (2015)'s reported relationship. Conversely, we use scale analysis in Equations (3) through (7) with assumptions about and approximations for relevant length and time scales for a small flat island to demonstrate more directly that one might expect the relationship $w_{CT} \propto H^1$, a result we support with experimental data on a small island.

However, in our scale analysis, we assume that the boundary layer depth is not materially altered during passage over a small island. This assumption is not necessarily appropriate for a larger island like Dominica as studied by Kirshbaum and Fairman (2015). Given the same flow, air has a longer residence time over a larger island, and therefore more substantial changes to the boundary layer depth can occur. It can be shown that the boundary layer depth grows as the square root of the cumulative heating input which depends on this residence time (e.g., Garratt, 1990). We speculate that refining our approximation to account for the modification of the boundary layer depth as the flow crosses the island would yield $w_{CT} \propto H^{0.5}$. While more conclusive analysis on this discrepancy is outside the aims and scope of the present work, additional experimentation could be designed to confirm the nature of this relationship.

AUTHOR CONTRIBUTIONS

Michael C. Johnston: Conceptualization; data curation; formal analysis; investigation; methodology; project administration; visualization; writing – original draft; writing – review and editing. **Christopher E. Holloway:** Conceptualization; funding acquisition; methodology; project administration; resources; supervision; validation; writing – original draft; writing – review and editing. **Robert Plant:** Conceptualization; data curation; funding acquisition; methodology; project administration; resources; supervision; validation; writing – original draft; writing – review and editing.

ACKNOWLEDGEMENTS

The authors would like to acknowledge helpful comments from Louise Nuijens, Miguel Teixeira, and Andrew Turner. Their perspectives and feedback were provided at varying stages of the preparation of this work as part of the PhD thesis submission for Michael Johnston. This work used the ARCHER UK National Supercomputing Service, http://www.archer.ac.uk.

FUNDING INFORMATION

NERC/Met Office (RevCon) NE/N013743/1.

DATA AVAILABILITY STATEMENT

A subset of the data is available as a dataset in Zenodo (2023, doi:10.5281/zenodo.7826073). The extended dataset is available on request and may be in long-term elastic tape storage via JASMIN.

ORCID

Michael C. Johnston https://orcid.org/0000-0003-0320-7149
Christopher E. Holloway https://orcid.org/0000-0001-9903-8989
Robert S. Plant https://orcid.org/0000-0001-8808-0022

REFERENCES

Bhumralkar, C.M. (1973) An observational and theoretical study of atmospheric flow over a Heated Island: part I. *Monthly Weather Review*, 101, 719–730.

Bolton, D. (1980) The computation of equivalent potential temperature. *Monthly Weather Review*, 108, 1046–1053.

Boutle, I.A., Eyre, J.E.J. and Lock, A.P. (2014) Seamless stratocumulus simulation across the turbulent gray zone. *Monthly Weather Review*, 142, 1655–1668.

Bush, M., Allen, T., Bain, C., Boutle, I., Edwards, J., Finnenkoetter, A., Franklin, C., Hanley, K., Lean, H., Lock, A., Manners, J., Mittermaier, M., Morcrette, C., North, R., Petch, J., Short, C., Vosper, S., Walters, D., Webster, S., Weeks, M., Wilkinson, J., Wood, N. and Zerroukat, M. (2000) The first met Office unified model/JULES regional atmosphere and land configuration, RAL1. *Geoscientific Model Development Discussion*, 2019, 13, 1999–2029.

Cheng, A., Xu, K.-M. and Stevens, B. (2010) Effects of resolution on the simulation of boundary-layer clouds and the partition of kinetic energy to subgrid scales. *Journal of Advances in Modeling Earth Systems*, 2, 1–21.

Cotton, W.R. and Anthes, R.A. (1989) *Storm and Cloud Dynamics*. San Diego, CA: Academic.

Davies, T., Cullen, M.J.P., Malcolm, A.J., Mawson, M.H., Staniforth, A., White, A.A. and Wood, N. (2005) A new dynamical Core for the met Office's global and regional modelling of the atmosphere. *Quarterly Journal of the Royal Meteorological Society: A Journal of the Atmospheric Sciences, Applied Meteorology and Physical Oceanography*, 131, 1759–1782.

Dee, D.P., Uppala, S.M., Simmons, A.J., Berrisford, P., Poli, P., Kobayashi, S., Andrae, U., Balmaseda, M.A., Balsamo, G., Bauer,

P., Bechtold, P., Beljaars, A.C.M., van de Berg, L., Bidlot, J., Bormann, N., Delsol, C., Dragani, R., Fuentes, M., Geer, A.J., Haimberger, L., Healy, S.B., Hersbach, H., Hólm, E.V., Isaksen, L., Kållberg, P., Köhler, M., Matricardi, M., McNally, A.P., Monge-Sanz, B.M., Morcrette, J.J., Park, B.K., Peubey, C., de Rosnay, P., Tavolato, C., Thépaut, J.N. and Vitart, F. (2011) The ERA-interim reanalysis: configuration and performance of the data assimilation system. *Quarterly Journal of the Royal Meteorological Society: A Journal of the Atmospheric Sciences, Applied Meteorology and Physical Oceanography*, 137, 553–597.

Garratt, J.R. (1990) The internal boundary layer—a review. *Boundary-Layer Meteorology*, 50, 171–203.

Garstang, M., Tyson, P.D. and Emmitt, G.D. (1975) The structure of Heat Islands. *Reviews of Geophysics*, 13, 139–165.

Grabowski, W.W., Bechtold, P., Cheng, A., Forbes, R., Halliwell, C., Khairoutdinov, M., Lang, S., Nasuno, T., Petch, J., Tao, W.K., Wong, R., Wu, X. and Xu, K.M. (2006) Daytime convective development over land: a model Intercomparison on LBA observations. *Quarterly Journal of the Royal Meteorological Society: A Journal of the Atmospheric Sciences, Applied Meteorology and Physical Oceanography*, 132, 317–344. https://doi.org/10.1256/qj.04.147

Honnert, R., Efstathiou, G.A., Beare, R.J., Ito, J., Lock, A., Neggers, R., Plant, R.S., Shin, H.H., Tomassini, L. and Zhou, B. (2020) The atmospheric boundary layer and the gray zone of turbulence: a critical review. *Journal of Geophysical Research*, 125, e2019JD030317.

Jahn, M., Muñoz-Esparza, D., Chouza, F., Reitebuch, O., Knoth, O., Haarig, M. and Ansmann, A. (2016) Investigations of boundary layer structure, cloud characteristics, and vertical mixing of aerosols at Barbados with large Eddy simulations. *Atmospheric Chemistry and Physics*, 16, 651–674.

Johnston, M. C., 2020. Island Convection and its Representation in Numerical Weather Prediction Models. Thesis, University of Reading, Department of Meteorology.

Johnston, M.C., Holloway, C.E., and Plant, R.S. (2018) Cloud trails past Bermuda: a five-year climatology from 2012 to 2016. *Monthly Weather Review*, 146, 4039–4055.

Kirshbaum, d.J. (2013) On thermally forced circulations over Heated Islands. *Journal of the Atmospheric Sciences*, 70, 1690–1709.

Kirshbaum, D.J. and Fairman, J.G. (2015) Cloud trails past the Lesser Antilles. *Monthly Weather Review*, 143, 995–1017.

Lilly, D. K., 1967. On the Application of the Eddy Viscosity Concept in the Inertial Subrange of Turbulence. *NCAR Ms. No. 123 Boulder, CO*.

Lin, Y.-L. (2007) Orographically forced flows. In: *Mesoscale Dynamics*. s.l: Cambridge University Press, p. 630.

Lock, A.P., Brown, A.R., Bush, M.R., Martin, G.M. and Smith, R.N.B. (2000) A new boundary layer mixing scheme. Part I: scheme description and single-column model tests. *Monthly Weather Review*, 128, 3187–3199.

Malkus, J. (1963) Tropical rain induced by a small natural heat source. *Journal of Applied Meteorology*, 2, 547–556.

Matthews, S., Hacker, J.M., Cole, J., Hare, J., Long, C.N. and Reynolds, R.M. (2007) Modification of the atmospheric boundary layer by a Small Island: observations from Nauru. *Monthly Weather Review*, 135, 891–905.

Nordeen, M.K., Minnis, P., Doelling, D.R., Pethick, D. and Nguyen, L. (2001) Satellite observations of cloud plumes generated by Nauru. *Geophysical Research Letters*, 28, 631–634.

Savijarvi, H. and Matthews, S. (2004) Flow over small Heat Islands: a numerical sensitivity study. *Journal of the Atmospheric Sciences*, 61, 859–868.

Smagorinsky, J. (1963) General circulation experiments with the primitive equations. *Monthly Weather Review*, 91, 99–164.

Stevens, D.E., Ackerman, A.S. and Bretherton, C.S. (2002) Effects of domain size and numerical resolution on the simulation of shallow cumulus convection. *Journal of the Atmospheric Sciences*, 59, 3285–3301.

Yang, Y., Xie, S.-P. and Hafner, J. (2008) Cloud patterns lee of Hawaii Island: a synthesis of satellite observations and numerical simulations. *Journal of Geophysical Research*, 113, D15126.

How to cite this article: Johnston, M.C., Holloway, C.E. & Plant, R.S. (2023) Sensible heat fluxes control cloud trail strength. *Quarterly Journal of the Royal Meteorological Society*, 149(753), 1165–1179. Available from: https://doi.org/10.1002/qj.4438

APPENDIX A

A.1 Model idealizations

A.1.1 Geostrophic forcing

The momentum equation is modified to represent the effect of large-scale pressure gradients which cannot be modeled with periodic boundary conditions and therefore maintain the intended winds. This is achieved by adding a geostrophic forcing tendency as follows:

$$Q_u = f\left(v - v_g\right), \tag{A1a}$$

$$Q_v = -f\left(u - u_g\right), \tag{A1b}$$

where f is the Coriolis parameter (s^{-1}), Q_u and Q_v are forcing tendencies in the zonal and meridional momentum equations respectively, u and v are the corresponding wind components and u_g and v_g the components of the prescribed geostrophic wind. For the experiments presented here, v_g is prescribed as zero at all heights, while u_g is prescribed as $-10\ m{\cdot}s^{-1}$ between 0 and 9 km, tends linearly to zero between 9 and 15 km, and is zero above 15 km. Given the capping inversion near 3 km, the convective cloud is confined below that height and the wind profile above that height is assumed to be less important.

A.1.2 Subsidence tendencies

A vertical profile of vertical velocity is prescribed to represent the effects of large-scale subsidence that is, via large-scale gradients in the horizontal wind and continuity which cannot be modeled with periodic boundary conditions. The subsidence profile increases from zero at the surface to a first peak of $w = -0.603\ cm \cdot s^{-1}$ at 857 m

(just above the top of the boundary layer). Subsidence then decreases slightly through the cloud layer (with typical values near $-0.3\ \mathrm{cm}\cdot\mathrm{s}^{-1}$ within the cloud layer), before increasing to a second peak of $-0.418\ \mathrm{cm}\cdot\mathrm{s}^{-1}$ near the top of the cloud layer at 3,217 m. This double peak structure comes from ERA-interim reanalysis data (Dee *et al.*, 2011) taken on the case day and time to match the radiosonde profile used to initialize the experiments. The subsidence profile tends linearly with height towards zero at 4,326 m and is zero above. The prescribed subsidence acts on the vertical gradients of liquid potential temperature, θ_l, and total water content, q_T, to warm and dry the domain via tendencies as follows:

$$\left.\frac{\partial \phi}{\partial t}\right|_{\text{subs}} = -w_{\text{subs}}\frac{\partial \phi}{\partial z}, \tag{A2}$$

where ϕ is either θ_l or q_T, subscript "subs" represents tendency due to subsidence, and w_{subs} is the prescribed subsidence profile.

A.1.3 Radiative cooling

Furthermore, a prescribed radiative cooling profile is employed to reduce computation times and simplify finding equilibrium by reducing modeled degrees of freedom. A cooling profile of $2\ \mathrm{K}\cdot\mathrm{day}^{-1}$ is prescribed between the surface and the top of the cloud layer, near 3,217 m. It tends linearly to zero cooling between 3,217 and 4,326 m such that it acts over the same depth as the subsidence forcing. Subsidence acting on the vertical thermodynamic profiles results in warming which this radiative cooling profile is intended to balance.

A.1.4 Surface fluxes

Surface fluxes are prescribed everywhere. This is both for simplicity and for ease of experimentation. Over the sea, the heat fluxes are prescribed to be constant in time and uniform at $H = 1.5$ and $167.2\ \mathrm{W}\cdot\mathrm{m}^{-2}$. These values have been obtained from a spin-up simulation described in Section 2.2 of the main text. Over the island, a diurnal cycle of surface fluxes is imposed, as described in Section 2.1 of the main text. The peak heating of the diurnal cycle is varied in our experiments outlined in Table 1.